catalysts

MDPI

Article

Cu Modified TiO_2 Catalyst for Electrochemical Reduction of Carbon Dioxide to Methane

Akihiko Anzai [1], Ming-Han Liu [1], Kenjiro Ura [2], Tomohiro G. Noguchi [1], Akina Yoshizawa [1], Kenichi Kato [3], Takeharu Sugiyama [4] and Miho Yamauchi [1,5,6,7,*]

[1] International Institute for Carbon-Neutral Energy Research (WPI-I2CNER), Kyushu University, 744 Motooka, Nishi-ku, Fukuoka 819-0395, Japan; anzai@i2cner.kyushu-u.ac.jp (A.A.); liu.ming-han.591@m.kyushu-u.ac.jp (M.-H.L.); noguchi@i2cner.kyushu-u.ac.jp (T.G.N.); yoshizawa@i2cner.kyushu-u.ac.jp (A.Y.)
[2] Department of Chemistry, Graduate School of Science, Kyushu University, 744 Motooka, Nishi-ku, Fukuoka 819-0395, Japan; urajiro.ichi.21@outlook.jp
[3] RIKEN SPring-8 Center, 1-1-1 Kouto, Sayo-cho, Sayo-gun 679-5148, Japan; katok@spring8.or.jp
[4] Research Center for Synchrotron Light Applications, Kyushu University, 6-1 Kasuga-koen, Kasuga 816-8580, Japan; sugiyama@rcsla.kyushu-u.ac.jp
[5] Institute for Materials Chemistry and Engineering (IMCE), Kyushu University, 744 Motooka, Nishi-ku, Fukuoka 819-0395, Japan
[6] Advanced Institute for Materials Research (WPI-AIMR), Tohoku University, 2-1-1 Katahira, Aoba-ku, Sendai 980-8577, Japan
[7] Research Center for Negative Emissions Technologies (K-Nets), Kyushu University, Motooka 744, Nishi-ku, Fukuoka 819-0395, Japan
* Correspondence: yamauchi@ms.ifoc.kyushu-u.ac.jp

Citation: Anzai, A.; Liu, M.-H.; Ura, K.; Noguchi, T.G.; Yoshizawa, A.; Kato, K.; Sugiyama, T.; Yamauchi, M. Cu Modified TiO_2 Catalyst for Electrochemical Reduction of Carbon Dioxide to Methane. *Catalysts* **2022**, *12*, 478. https://doi.org/10.3390/catal12050478

Academic Editor: Kulbir Ghuman

Received: 11 March 2022
Accepted: 21 April 2022
Published: 23 April 2022

Abstract: Electrochemical reduction of CO_2 (ECO_2R) is gaining attention as a promising approach to store excess or intermittent electricity generated from renewable energies in the form of valuable chemicals such as CO, HCOOH, CH_4, and so on. Selective ECO_2R to CH_4 is a challenging target because the rate-determining step of CH_4 formation, namely CO* protonation, competes with hydrogen evolution reaction and the C–C coupling toward the production of longer-chain chemicals. Herein, a Cu-TiO_2 composite catalyst consisting of CuO_x clusters or Cu nanoparticles (CuNPs), which are isolated on the TiO_2 grain surface, was synthesized using a one-pot solvothermal method and subsequent thermal treatment. The Cu-TiO_2 catalyst exhibited high selectivity for CH_4, and the ratio of FE for CH_4 to total FE for all products in ECO_2R reached 70%.

Keywords: electrochemical reduction of CO_2; Cu; TiO_2

1. Introduction

Electrochemical reduction of CO_2 (ECO_2R), which uses renewable electricity to produce fuels and chemical feedstocks from CO_2, has attracted attention not only as an eco-friendly material synthesis process but also as a novel method to store intermittent renewable electricity which is generated from renewable energies such as solar, wind power, and so on [1]. Among metal catalysts, Cu is known to exhibit the highest activity in ECO_2R [2] and also produces multi-carbon products such as hydrocarbons and alcohols. Meanwhile, the selective production of CH_4, which is widely used as a fuel, is a demanding task but has not been achieved to the desired level in ECO_2R employing active Cu catalysts.

CH_4 formation proceeds through the addition of 8 electrons and 8 protons to CO_2 (Equation (1)).

$$CO_2 + 8H^+ + 8e^- \rightarrow CH_4 + 2H_2O \tag{1}$$

In this process, CH_4 formation is thought to occur via *CHO formation by protonation of *CO [3]. The *CHO formation competes with both the C–C coupling of two *CO and hydrogen evolution reaction (HER), which significantly lowers selectivity for the production of CH_4. Recently, the formation of isolated Cu sites has been found to effectively improve the selectivity for the CH_4 production by suppressing the unfavorable C–C coupling [4,5]. However, the selectivity for the production of CH_4 from CO_2 (CO_2 to CH_4 selectivity) should be improved. The increase of surface area is found to efficiently suppresses the Cu agglomeration on a support material such as carbons [6] and oxides [4,7,8]. However, the formation relatively large Cu portions where C–C couplings preferentially progress cannot be suppressed in conventional impregnation synthesis.

Titanium dioxide (TiO_2) is a multifunctional material with many advantages, being ubiquitous, low-cost, and environmentally friendly. TiO_2 is a widely used catalyst material for various application [9] due to its high activity and adequate stability. Recently, we have uncovered relatively high overpotentials for electrochemical H_2 evolution and the favorable interactions of oxygen species included in organic acids, oximes, and imines with the surface of TiO_2-based catalysts for electrochemical hydrogenation [10–18], which could enhance the selectivity for the production of CO_2-derived chemicals in ECO_2R. Highly dispersed and isolated Cu sites on TiO_2 are expected to suppress the generation of multi-carbon products and show high selectivity for CH_4 synthesis. Thus, we develop Cu-TiO_2 catalysts presenting isolated Cu sites with high dispersion for the selective CH_4 production by the electrochemical reduction of CO_2.

2. Results

To enhance their dispersivity, Cu-TiO_2 catalysts were prepared via a one-pot solvothermal method (See Section 4). The crystal structures of the prepared TiO_2, Cu-TiO_2, and Cu-TiO_2 treated with H_2 (Cu-TiO_2-H) were examined by X-ray diffraction (XRD) (Figure 1 and Figure S1). All samples showed a diffraction pattern mostly attributable to an anatase phase of TiO_2, but a very small peak from a brookite phase was also observed at 14.7°. The intensity of the brookite peak of Cu-TiO_2 seemed slightly large compared to that in the XRD pattern of TiO_2. It has been reported that the formation of brookite phase preferentially occurs in alkaline conditions. The usage of DMF as an alkalescent organic solvent probably induces the formation of brookite phase [19–21]. No diffraction peaks from copper oxides such as Cu_2O or CuO were observed in the Cu-TiO_2, despite the introduction of Cu. In contrast, Cu-TiO_2-H showed a diffraction peak from Cu. It is notable that no shift in the diffraction peak position of the anatase phase was observed in either Cu-TiO_2 or Cu-TiO_2-H, although the ionic radii of the 6-coordinated Ti^{4+} ions (0.605 Å) and Cu^{2+} ions (0.73 Å) are different and a Cu^{2+} ion is larger than that of a Ti^{4+} ion [22], which suggests that most of the Cu species are precipitated over the TiO_2 surface as CuO_x clusters on Cu-TiO_2, where the clusters are too small to be detected by XRD, and as Cu nanoparticles (NPs) on Cu-TiO_2-H, rather than being enclosed in the TiO_2 lattice. To obtain detailed structural parameters for the catalysts, we conducted Rietveld profile fitting of these XRD patterns (Figure S1). Structural parameters are summarized in Table S1. The lattice constants of anatase phase constituting Cu-TiO_2 and Cu-TiO_2-H showed a slight increase in the *a*-axis but a slight decrease in the *c*-axis compared to those of pure TiO_2, suggesting the possibility of incorporation of Cu species into the TiO_2 lattice. The weight fraction of Cu species deposited on TiO_2 was estimated by the Rietveld analysis to be low (1.9%), even though the initial starting amount was 10%. Considering the slight change in the structure of Cu-TiO_2 and Cu-TiO_2-H, a relatively large percentage of Cu species (more than 5%) possibly exists as amorphous on the surface of TiO_2.

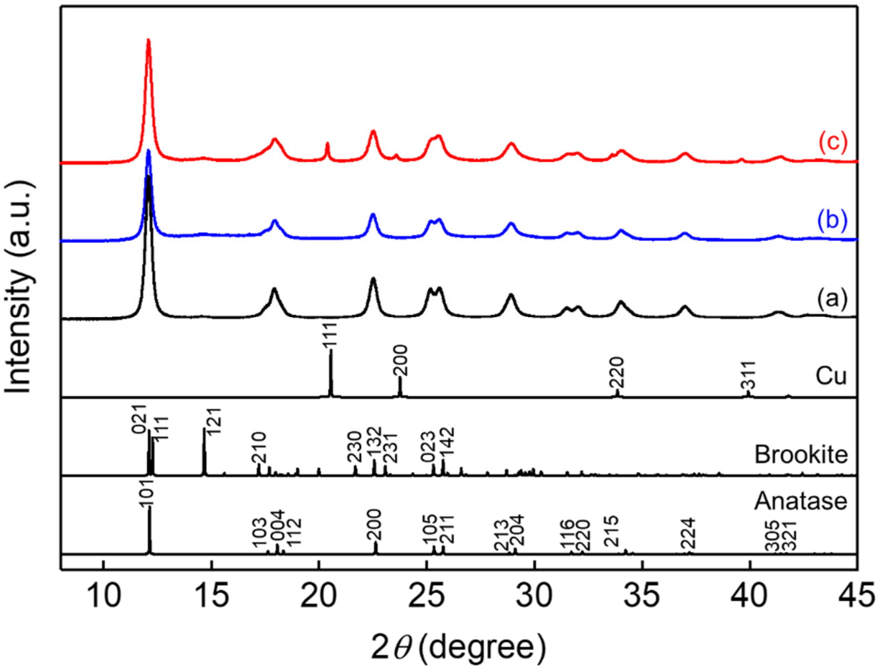

Figure 1. XRD patterns of (**a**) TiO_2, (**b**) Cu-TiO_2, and (**c**) Cu-TiO_2-H. The simulated XRD patterns of anatase, brookite, and Cu are also presented.

To confirm the oxidation state of Cu on Cu/TiO_2, the diffuse reflectance UV-Vis spectra of the catalyst were measured (Figure 2). The inset represents the Tauc plots [23,24] where the (F(R) $hv)^{1/2}$ is plotted as a function of photon energy. The indirect band gap was estimated from an X-intercept of a linear fit of the Tauc plot, and the determined band gap values are also given in the inset. The band gap energy of TiO_2 was estimated to be 3.10 eV, which is slightly small compared to the reported value of anatase TiO_2 [25]. Cu-TiO_2 showed a large red-shift in optical absorption edge compared to that of TiO_2, with an estimated band gap of 1.46 eV, which occurs probably by interaction between CuO and TiO_2. Furthermore, absorption bands appeared in the region of 400–600 nm and 600–1200 nm. The former absorption band is assignable to the interfacial charge transfer from a TiO_2 O 2p valence band to a Cu(II) ions connected to TiO_2 [26], whereas the latter comes from a d–d transition of Cu (II) species [27]. These Cu(II) states may exist either as Cu(II) clusters or amorphous oxide grains of CuO. Cu-TiO_2-H exhibited a remarkably larger red-shift of the absorption edge in optical absorption than Cu-TiO_2 and with 1.16 eV of band gap, revealing good contact between Cu and TiO_2 grains. Additional absorption bands appeared in the region of 400–600 nm and 550–1200 nm. The former absorption band was assigned to the interfacial charge transfer from the TiO_2 O 2p valence band to the Cu(II) ions attached to TiO_2 [26], whereas the latter band was attributable to the Cu surface plasmon resonance of Cu NPs [28–30]. Therefore, we confirmed the formation of Cu NPs in these catalysts from the XRD and DRS results.

To investigate the dispersion of Cu NPs on TiO_2, we conducted scanning transmission electron micrography (STEM) for Cu-TiO_2-H. A high-angle annular dark-field STEM (HAADF-STEM) image of the Cu-TiO_2-H (Figure 3) suggested that Cu NPs with a diameter of 2–3 nm, which appear as white dot-like objects, were well dispersed over a TiO_2 grain, indicating that isolated Cu clusters are formed in Cu-TiO_2-H. On the other hand, Cu-TiO_2 (Figure S2) suggested that Cu NPs with a diameter of 2–5 nm, which appear as white aggregated objects, existed in a TiO_2 grain, indicating that larger Cu NPs are formed in Cu-TiO_2 compared to Cu-TiO_2-H.

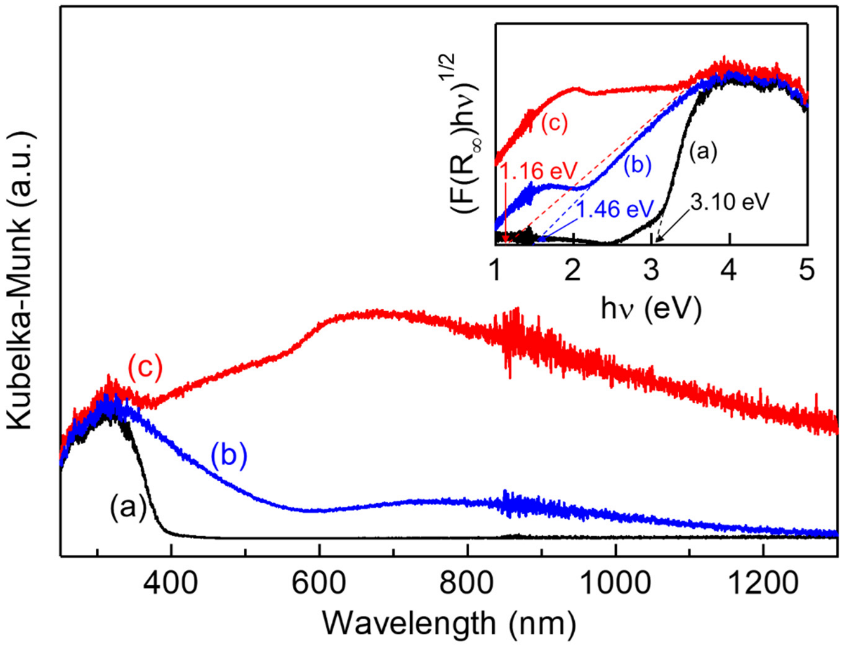

Figure 2. Diffuse reflectance spectra of (**a**) TiO_2, (**b**) Cu-TiO_2, and (**c**) Cu-TiO_2-H samples. The inset is the Tauc plots for the determination of the bandgap of the samples.

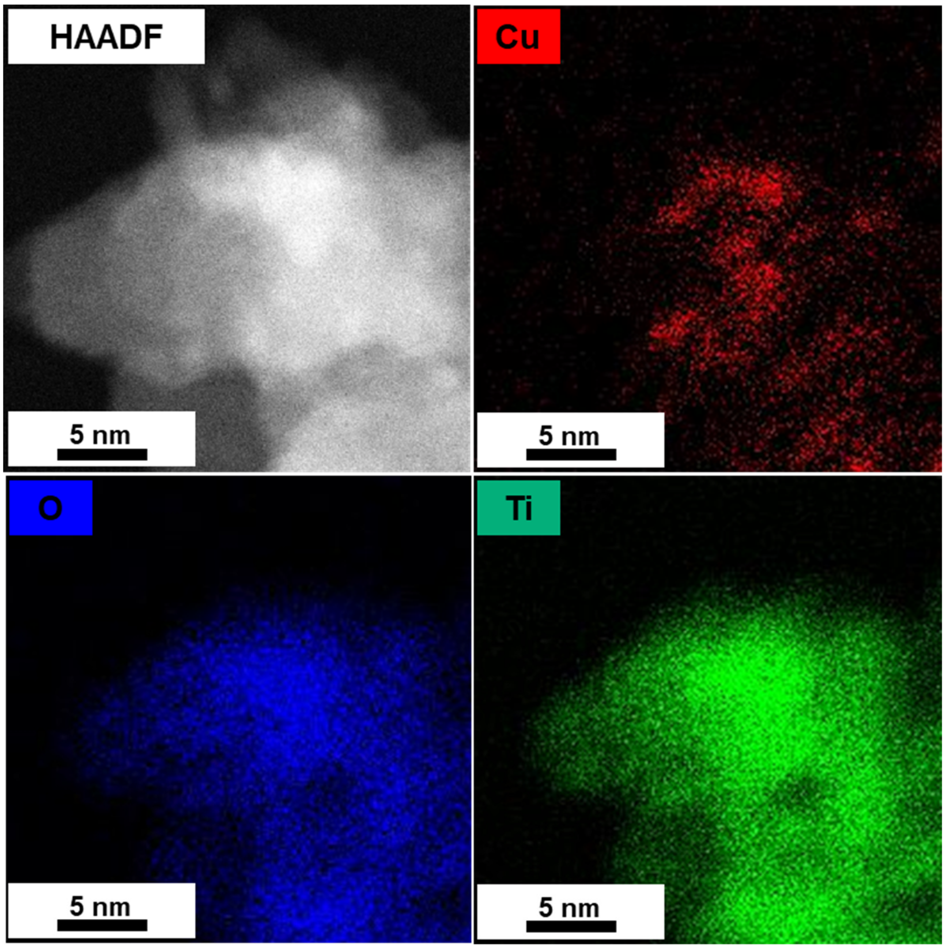

Figure 3. High-angle annular dark-field scanning transmission electron microscopy (HAADF-STEM) image and EDS mapping images of Cu-TiO_2-H.

Figure 4 provides Cu $2p_{3/2}$ XPS spectra of Cu-TiO_2 and Cu-TiO_2-H. A relatively broad Cu 2p3/2 XPS peak centered at 932.5 eV and the shoulder peak near 934.3 eV in the high binding energy side were observed on Cu-TiO_2. The main and the shoulder peaks could be attributed to Copper oxide containing Cu(I) and Cu(II), and $Cu(OH)_2$ [31] species, respectively, which implies that Cu clusters in Cu-TiO_2 are composed of Cu(I) and Cu(II). Furthermore, the presence of a well known shake-up satellite at higher binding energies than that for the main peak strongly indicates the presence of Cu(II) species in Cu-TiO_2 [32]. Therefore, Cu clusters in Cu-TiO_2 may exist mainly as CuO-like and $Cu(OH)_2$-like species. Cu-TiO_2-H showed the sharp Cu 2p3/2 peak centered at 932.6 eV, which is attributed to the formation of Cu(0). The absence of the shake-up satellite, as observed in Cu-TiO_2, suggests that Cu NPs on Cu-TiO_2-H are mainly composed of Cu(0) species, which is consistent with the observation in the XRD measurement for Cu-TiO_2-H. Figure S3A shows Ti 2p XPS spectra of TiO_2, Cu-TiO_2, and Cu-TiO_2-H. All catalysts exhibited a symmetrical peak centered around 458.6 eV, which is a typical peak with characteristic binding energy value for Ti^{4+} ions contained in anatase TiO_2 [33], although the spectrum of TiO_2 had a slightly extended tail which possibly comes from the formation of Ti^{3+}. There was also no obvious peak shift in these catalysts. Therefore, Ti ions near the surface of all catalysts would have an analogous chemical environment. Figure S3B represents O1s peaks at around 529.7 eV in XPS spectra of TiO_2, Cu-TiO_2, and Cu-TiO_2-H, which are assigned to lattice oxygen of TiO_2 [33]. In addition, each spectrum contained two other weak shoulder peaks on the higher binding energy side of the main O 1s peak. The former peak observed at 530.8 eV can be attributed to the hydroxide group or water molecules that are present at the surface [34], and the other peak at 531.9 eV is originated from organic contaminants containing oxygen species [35]. Cu-TiO_2-H showed a relatively large peak at 530.8 eV, which is attributed to the existence of hydroxide groups or water molecules. Chalastara et al. reported that a brookite-rich sample has a larger amount of surface-bound OH/H_2O groups than anatase-rich samples [36]. The increase of intensity at 530.8 eV indicates the increase of a brookite phase in Cu-TiO_2-H. The number of defects such as Ti^{3+} and oxygen vacancy on the surface of these catalysts did not change so much by the introduction of Cu or by the change of the atmosphere during heating. The all-measured core level positions for the samples are summarized in Table S2.

The difference in Cu state between Cu-TiO_2 and Cu-TiO_2-H was further examined by the measurement of Cu-K edge X-ray absorption near edge structure (XANES) spectra using a conversion electron yield (CEY) method, which reflects information on the species near surface region due to the shallow escape depth of Auger electrons from an atom irradiated by X-rays within a sample [37]. Figure 5 shows XANES spectra of Cu-TiO_2 and Cu-TiO_2-H, and standard samples such as Cu foil, Cu_2O, and CuO. Small pre-edge bumps at 8978 eV were observed on Cu-TiO_2 and CuO, which is attributed to dipole-forbidden 1s → 3d transition and is indicative of existence of Cu^{2+} ions, implying that the surface of Cu-TiO_2 contains Cu(II) ions. Cu-TiO_2-H showed an XANES spectrum similar to that of Cu foil, suggesting that the Cu species on the surface of Cu-TiO_2-H are Cu(0) species. XANES spectra were further analyzed in detail. The first derivatives of the XANES spectrum of CuO gave a small pre-edge bump at 8978 eV for the 1s → 3d transition [38], peak for the 1s → 4p transition [39,40] (Figure 5). The spectrum also showed a small pre-edge bump at 8978 eV attributed to the 1s → 3d transition, but the spectral features in the region related to the 1s → 4p transition were significantly different from those of CuO, meaning that the oxidation state of Cu on Cu-TiO_2 is different from that of CuO, although it includes Cu(II) species. The red shift and increase in intensity of the 1s → 4p peak was interpreted as an increase of covalency in the ligand−copper bond [40]. Cu(II) states on Cu-TiO_2 may emerge as $Cu(OH)_2$-like species, which is consistent with the observation in the XPS measurement for Cu-TiO_2. The first derivative spectra of Cu-TiO_2-H and Cu foil look similar, indicating that Cu(0) is the main oxidation state of Cu species in Cu-TiO_2-H, which is consistent with all observations discussed above.

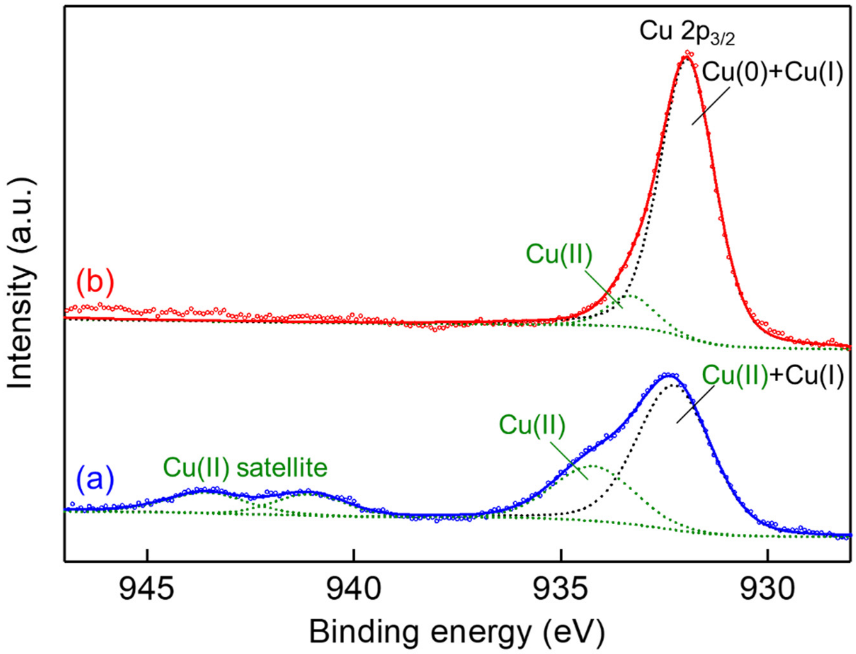

Figure 4. Deconvoluted Cu $2p_{3/2}$ XPS spectra of Cu-TiO_2 (**a**) and Cu-TiO_2-H (**b**). The observed spectra, fitting curves, calculated patterns, and deconvoluted curves are denoted by circle, solid line, and dashed line, respectively.

Figure 6A shows linear sweep voltammetry (LSV) curves under CO_2 flow for TiO_2, Cu-TiO_2, and Cu-TiO_2-H. Cu-TiO_2-H exhibited a higher current density than the other two catalysts, meaning that the formation of Cu NPs on TiO_2 increases ECO_2R activity. All catalysts produced H_2, CO, CH_4, and C_2H_4 as gaseous products, which were detected by online gas chromatography. We could not observe other gaseous product such as HCOOH. Only $HCOO^-$ was detected in the liquid phase by HPLC analysis, as shown in Figures S4–S6. TiO_2 mainly produced H_2 via the hydrogen evolution reaction (HER), and a small amount of $HCOO^-$, CO, and CH_4 were also produced, suggesting that TiO_2 does not show high activity for ECO_2R. On Cu-TiO_2, the percentage of CH_4 in the products increased and a tiny amount of C_2H_4 was also produced. This suggests that Cu(II) species are reduced to Cu(0) in Cu NPs under the potential and enhances ECO_2R activity. The measured total Faradaic efficiencies on the TiO_2 and Cu-TiO_2 sometimes became slightly higher than 100%, which has been explained by the experimental errors introduced by GC detection or inconsistencies in the flow rate, as shown in some reports [41–43]. Cu-TiO_2-H exhibited higher ECO_2R activity than TiO_2 and Cu-TiO_2, as shown in the LSV results. Faradaic efficiency for the production of CH_4 reached 18% with 36 mA cm^{-2} of partial current density at -1.8 V vs. RHE (Figure 6F), where CH_4 partial current density was defined as a product of the average total current density and the Faradaic efficiency for the production of CH_4 in ECO_2R at each potential. Notably, Faradaic efficiency for CH_4 production much increased at potentials more negative than -1.4 V, indicating that CO_2 is selectively converted to CH_4 with the applied potentials. To evaluate the selectivity for CH_4 formation, we further calculated the ratios of FE for CH_4 to total FE for all products in ECO_2R (FE_{CH4}/FE_{C1+C2}) on the catalysts at each potential (Figure 6E). Cu-TiO_2 and Cu-TiO_2-H showed larger FE_{CH4}/FE_{C1+C2} values than TiO_2. This result is probably attributable to Cu sites homogeneously dispersed on these catalysts. We achieved 70% of FE_{CH4}/FE_{C1+C2} at -1.8 V vs. RHE, which compares with prior reports related to highly dispersed or single-site copper catalysts (Table S3). On the other hand, Cu-TiO_2 and Cu-TiO_2-H showed different CH_4 partial current densities (Figure 6F (b) and (c)), although the selectivity for CH_4 in the products from CO_2, i.e., FE_{CH4}/FE_{C1+C2} over these catalysts looked similar (Figure 6E (b) and (c)). DRS results represented that the band gap of Cu-TiO_2-H is narrower than that of Cu-TiO_2 (Figure 2), which implies that Cu species on Cu-TiO_2-H have better contact with the TiO_2 support than those on Cu-TiO_2. Such favorable interactions between Cu catalysts and the TiO_2 support in Cu-TiO_2-H may enhance the electrical conductivity, resulting in its high CH_4 partial current density on Cu-TiO_2-H. These results indicate that Cu(0) loading on TiO_2 is indispensable and effective to enhance activity in the ECO_2R to CH_4. However, the state of catalysts under operating conditions are not well clarified and need to be further studied.

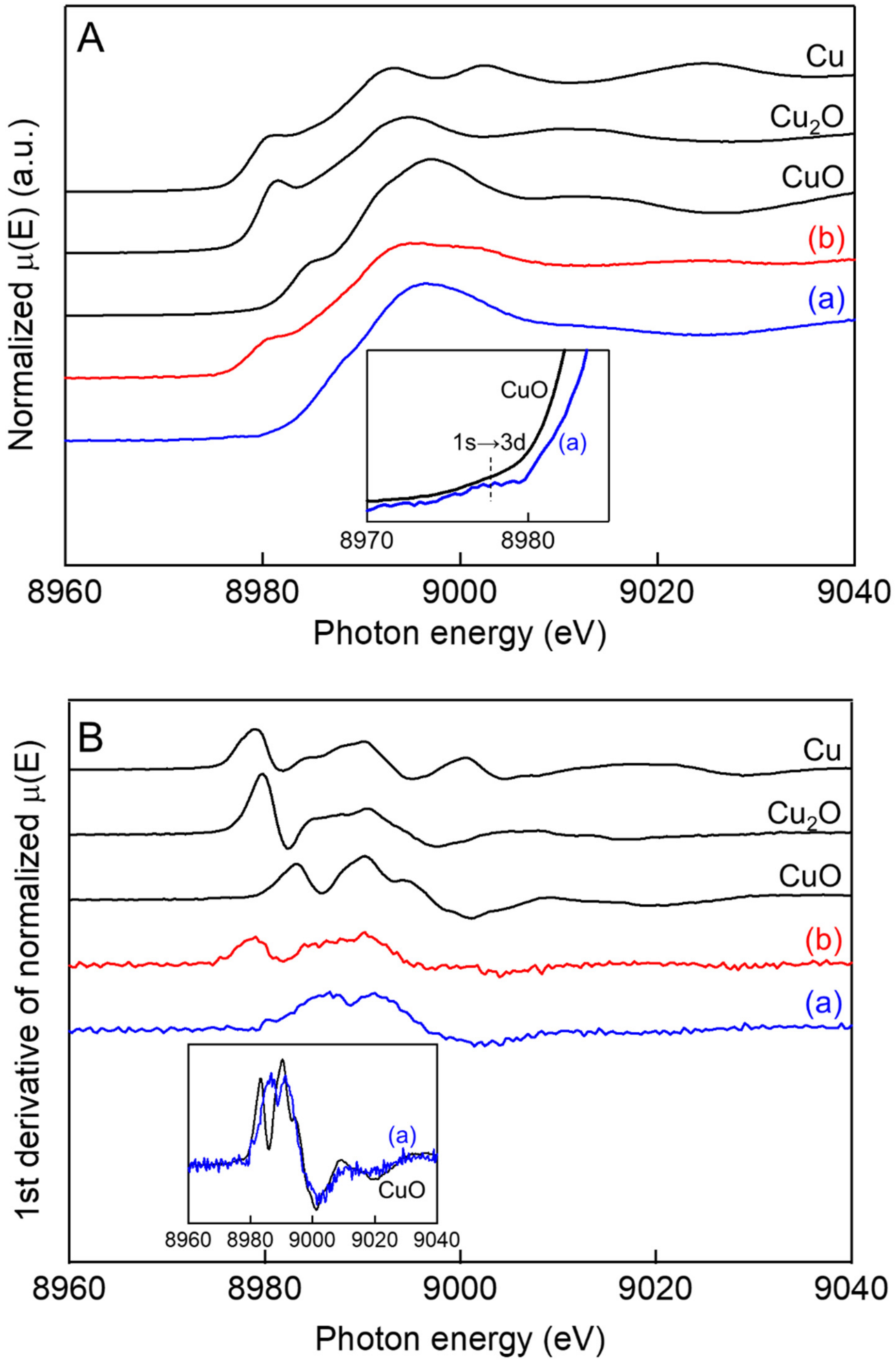

Figure 5. Cu K-edge spectra (**A**) and first derivative of Cu K-edge XANES spectra (**B**) of reference compounds. (a) Cu-TiO_2, (b) Cu-TiO_2-H. The inset figure shows overlay of the spectra of CuO and (a) Cu-TiO_2.

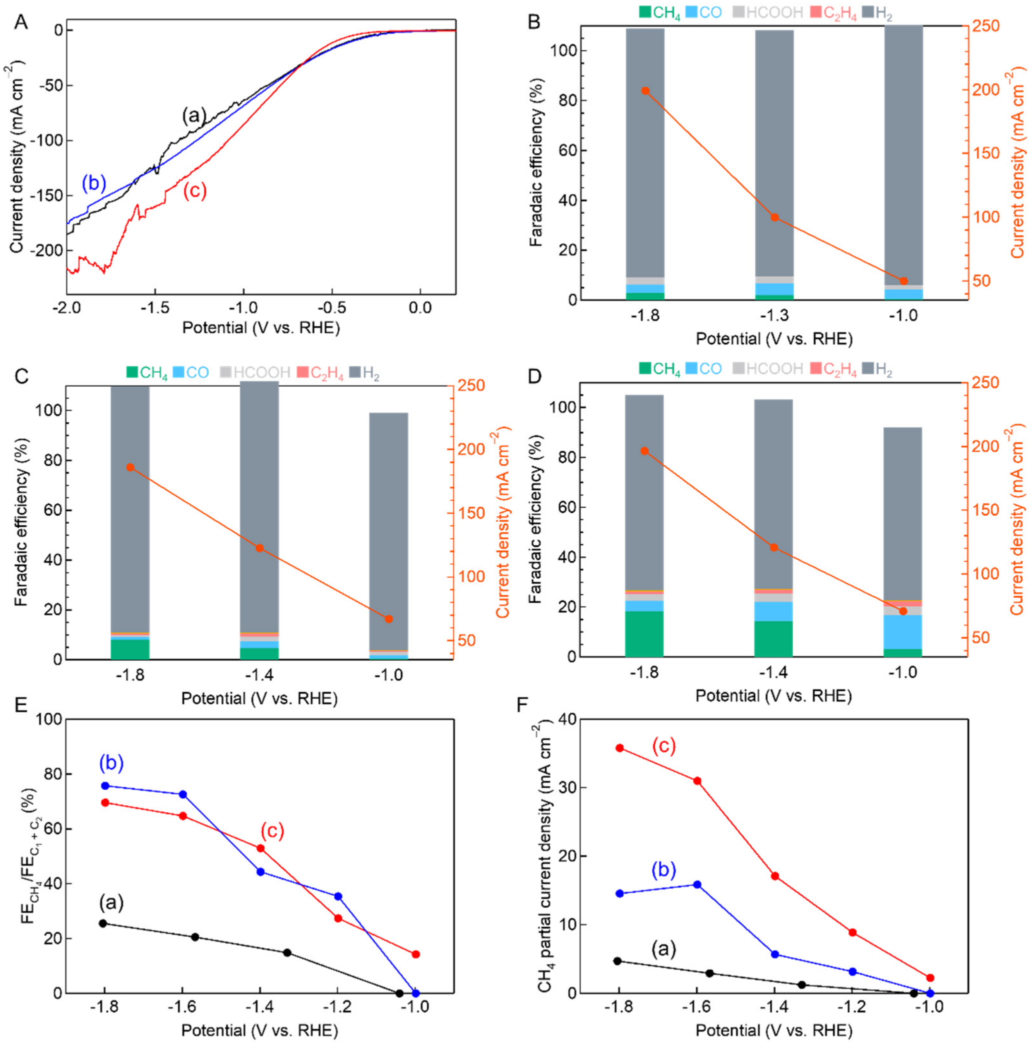

Figure 6. LSV curves under CO_2 flow (**A**) on an electrode employing (a) TiO_2, (b) Cu-TiO_2, and (c) Cu-TiO_2-H catalyst. FEs for different products over TiO_2 (**B**), Cu-TiO_2 (**C**), and Cu-TiO_2-H (**D**) catalysts at various potentials. Comparison of FE_{CH4}/FE_{C1+C2} (**E**) on (a) TiO_2, (b) Cu-TiO_2, and (c) Cu-TiO_2-H catalyst. Comparison of CH_4 partial current density (**F**) of (a) TiO_2, (b) Cu-TiO_2, and (c) Cu-TiO_2-H catalyst.

It has been reported that composite materials of Cu and CeO_2 exhibit high CH_4 selectivity [4,7,44,45], where abundant oxygen vacancy (V_O) sites on CeO_2 play an important role in both CO_2 adsorption and activation. Wang et al. suggested that Cu site surrounded by $3V_O$ effectively promoted CH_4 formation, where the $2V_O$ neighboring Cu are filled with the two oxygen atoms of CO_2 and should enhance the CO_2 adsorption and activation [4]. In this study, the surface of the prepared TiO_2 samples may consist of low concentration of V_O. CO_2 dissociation unfavorably occur on stoichiometric anatase surface compared to Vo-rich surface due to its large CO_2 dissociation energy [46]. HER mainly proceeded on the TiO_2 catalyst, although small amounts of C1 products, such as CO, $HCOO^-$, and CH_4, were generated (Figure 6B). In contrast, Cu-TiO_2 and Cu-TiO_2-H, where Cu(0) species were well dispersed over a TiO_2 grain, showed high selectively for the production of CH_4. Hence, well dispersed Cu species on TiO_2 would play a key role in the formation of CH_4. Therefore, it is reasonable that homogeneity of Cu NPs in their size and dispersity on TiO_2 can be a key for the high CO_2-to-CH_4 selectivity.

3. Materials and Methods

3.1. Materials

Titanium tetrabutoxide monomer (95.0%), anhydrous copper (II) acetate (97%), N,N-dimethylformamide (99.5%), 2-propanol (99.7%), ethanol (99.5%), acetone (95.5%), hexane (96.0%), and potassium hydroxide were purchased from FUJIFILM Wako Pure Chemical Corporation. Nafion® perfluorinated resin solution (5 wt% in mixture of lower aliphatic alcohols with a water content of 45%) was purchased from Sigma-Aldrich Corporation. All chemicals were used without further purification. All the solutions were prepared with deionized water.

3.2. Preparation of Cu-TiO$_2$ Composite Catalysts

For the preparation of Cu-TiO$_2$ composite catalyst, including 10 wt% of Cu species, titanium tetrabutoxide (2.8 mmol, 1 mL) was quickly added to a mixture of 30 mL of N,N-dimethylformamide (99.5%), 0.215 mL of 2-propanol, and 73 mg of anhydrous copper(II) acetate in a 50 mL Teflon-lined stainless-steel autoclave to avoid exposing the sample to the air, and the mixture was sonicated for 2 h at room temperature. The container was sealed, heated from room temperature to 200 °C over 30 min in an electrical oven, and maintained for 20 h. The product was separated by centrifugation 7500 rpm for 10 min and washed several times with ethanol, acetone, and hexane. After that, it was dried under vacuum at room temperature. Finally, the precursor was calcined at 450 °C for 30 min under air or flowing H$_2$ (60 mL min^{-1}) to obtain TiO$_2$ and Cu-TiO$_2$-x samples, where X is the calcination atmosphere, air or H$_2$; heating rate of 15 °C min^{-1}.

3.3. Catalyst Characterization

The metal composition of prepared oxides was determined using an energy dispersive X-ray spectroscope (EDS, JED-2300, JEOL) equipped with the SEM instrument. Powder X-ray diffraction (XRD) patterns were obtained using synchrotron radiation (λ = 0.740040 Å) at RIKEN Materials Science beamline BL44B2, SPring-8 [47]. Data were acquired using the high-resolution Debye–Scherrer camera equipped with an imaging plate as an X-ray detector. Rietveld analyses were performed using a Topas software package (Bruker AXS Inc., Billerica, MA, USA, version 5). The diffuse reflectance spectra of samples were recorded using a V-670 spectrometer (JASCO, Japan) equipped with an integrating sphere. The diffuse reflection spectra were converted into reflectance spectra using the Kubelka-Munk function. X-ray photoelectron spectroscopy (XPS) studies were performed on a VersaProbeII (ULVAC-PHI) using nonmonochromatic Al Ka radiation. Binding energies in XPS spectra were corrected by referring a C 1s binding energy of the carbon atoms of the ligand in the specimens at 284.6 eV. Scanning transmission electron microscopy (STEM) image was obtained using a JEM-ARM200F (JEOL Co., Tokyo, Japan) at Kyushu University operated at 200 kV. Sample grids for the STEM observations were prepared by dropping ethanol dispersions of the specimens onto a carbon-supported nickel grid. Cu K-edge X-ray absorption fine structure (XAFS spectra of the samples) was measured at Kyushu University beamline BL06 of Kyushu Synchrotron Light Research Center (SAGA-LS, Japan) with an electron storage ring operating at the energy of 1.4 GeV. The energy range of this light source (bending magnet) is 2.1–23 keV. A silicon (111) double-crystal monochromator was used to obtain the incident X-ray beam. The typical photon flux is 10^{10} photons per second. The spectra of standard samples such as Cu foil, Cu$_2$O, and CuO were recorded in the transmission mode at 20 °C using a Si(111) double-crystal monochromator. The spectra of Cu-TiO$_2$ samples were measured using the conversion electron yield mode. Data processing was carried out by Athena and Artemis included in the Ifeffit package [48].

3.4. Electrode Preparation

The cathode GDE was prepared by airbrushing catalyst inks onto a gas diffusion carbon paper (Fuel Cell Store Sigracet 22 BB, with a microporous layer) with a carrier gas of air. The catalyst ink was prepared with 200 µL of 2-propanol, 200 µL of water, 10 µL of Nafion® solution, and 1 mg of catalyst powder. The catalyst ink mixtures were sonicated in a 4 mL screw neck glass vial for 15 min, and then sprayed onto the gas diffusion carbon paper.

3.5. Electrochemical Reduction of CO_2

The electrochemical measurements were conducted in an electrochemical flow cell setup configuration with the three-electrode system. The geometric area of the cathode in the flow cell is 1 cm^2, which is used for all current density calculations. 1 M KOH aqueous solution was introduced into the cathode chamber at the rate of 7 mL min^{-1} and the anode chamber at the rate of 1 mL min^{-1} by two pumps, respectively. A Nafion 117 cation exchange membrane (Chemours ®) was used to separate the cathode chamber and anode chamber. Pure CO_2 gas (Linde, 99.99%) was continuously supplied to the gas chamber of the flow cell at a flow rate of 15 mL min^{-1}. The CO_2RR performance was tested using constant-current electrolysis, i.e., chronopotentiometry while purging CO_2 into the catholyte during the whole electrochemical test. The potentials vs. Hg/HgO reference electrode were converted to values vs. reversible hydrogen electrode (RHE) using the following equation [49].

$$\mathrm{E\ (vs.\ RHE) = E\ (vs.\ Hg/HgO) + 0.098\ V + 0.0591\ V \times pH} \tag{2}$$

All voltages reported are without *i*R compensation.

Gas products were analyzed by on-line gas chromatography (Micro GC Fusion®, Inficon, Bad Ragaz, Switzerland) with a Molsieve 5A column and a Plot Q column coupled with thermal conductivity detector (TCD). Liquid products were analyzed high performance liquid chromatograph (HPLC, LC-20AD, Shimadzu) equipped with a refractive-index detector (RID-10A, Shimadzu). The Faradaic efficiency (FE) of products in the electroreduction experiments is defined by the following equation:

$$FE_i = \frac{n_i \times z_i \times F}{Q} \times 100 \tag{3}$$

where n_i is the number of moles of product i, and z_i represents the number of electrons required for the formation of product i (z_i = 2 for CO, formic acid, and H_2; z_i = 8 for CH_4; z_i = 12 for C_2H_4; z_i = 14 for C_2H_6). F is the Faraday constant (96,485 C mol^{-1} of electrons). Q is the amount of charge passed during the electrolysis. For the gas products, n_i was calcurated as follows:

$$n_{i,\mathrm{gas}} = \frac{P_0 \times x_i \times v \times t}{R \times T} \tag{4}$$

where x_i is the volume fraction of gas product i; P_0 is atmospheric pressure (1 atm); v is the CO_2 flow rate (0.015 L min^{-1}); t is electrolysis time; R is the ideal gas constant (0.08205 L atm mol^{-1} K^{-1}); T is 298 K.

4. Conclusions

We successfully prepared Cu-TiO_2 composite catalysts, where Cu clusters or NPs were well dispersed by a one-pot solvothermal method and subsequent thermal treatment for electrochemical reduction for CO_2. For Cu-TiO_2 sample obtained by calcination of the precursor in air, CuO_x cluster were dispersed on TiO_2 surface and Cu NPs were formed on Cu-TiO_2-H obtained by hydrogen treatment of the precursor. Cu-TiO_2-H was found to exhibit high selectivity for CH_4 in ECO_2R. Faradaic efficiency for the CH_4 production reached 18% with a CH_4 partial current density of 36 mA cm^{-2} at −1.8 V vs. RHE. Furthermore, 70% of FE_{CH4}/FE_{C1+C2} at −1.8 V vs. RHE. was achieved. We conclude that homogeneity of the Cu NPs formed on TiO_2 is one of the necessary factors to maximize CH_4 selectivity in the ECO_2R.

Supplementary Materials: The following supporting information can be downloaded at: https://www.mdpi.com/article/10.3390/catal12050478/s1, Figure S1: Rietveld analysis results for XRD pattern for (a) TiO_2, (b) Cu-TiO_2, (c) Cu-TiO_2-H. The observed diffraction intensities, calculated patterns, and the difference between the observed and calculated intensity are denoted by red plus signs, a green solid line, and a blue solid line, respectively; Table S1: Structural parameters determined by Rietveld profile fitting for an XRD pattern of TiO_2, Cu-TiO_2 and Cu-TiO_2-H; Figure S2: High-angle annular dark-field scanning transmission electron microscopy (HAADF-STEM) image and EDS mapping images of Cu-TiO_2; Figure S3: Deconvoluted Ti 2p (A) and O 1s (B) XPS spectra of (a) TiO_2, (b) Cu-TiO_2, and (c) Cu-TiO_2-H. The observed spectra, fitting curves and calculated patterns, and deconvoluted curves are denoted by circle, solid line, and dashed line, respectively; Table S2: XPS peak positions and phase assignment of the TiO_2, Cu-TiO_2, and Cu-TiO_2-H samples; Figure S4: Example of a gas chromatogram (below: enlarged view in the region for CH_4 and CO) of H_2, CH_4, and CO obtained by electrochemical reduction of CO_2 using Cu-TiO_2-H catalyst on a Molsieve 5A column channel after chronoamperometry operation of 10 min at 1.8 V vs. RHE; Figure S5: Example of a gas chromatogram (below: enlarged view in the region for C_2H_4) of C_2H_4 obtained by electrochemical reduction of CO_2 using Cu-TiO_2-H catalyst on a Plot Q column channel after chronoamperometry operation of 10 min at 1.8 V vs. RHE; Figure S6: Example of a High Performance Liquid Chromatography (HPLC) of liquid products obtained by electrochemical reduction of CO_2 using Cu-TiO_2-H catalyst after chronoamperometry operation of 10 min at 1.8 V vs. RHE; Table S3: Electrochemical CO_2-to-CH_4 performance for studies related to highly dispersed or single-site copper catalysts [4,50–53].

Author Contributions: Methodology, validation, formal analysis, investigation, data curation, writing—original draft preparation, writing—review and editing, A.A.; Validation, investigation, data curation, M.-H.L.; Methodology, validation, formal analysis, investigation, data curation, K.U.; Validation, investigation, data curation, T.G.N.; Validation, investigation, data curation, A.Y.; Methodology, validation, formal analysis, investigation, data curation, K.K.; Methodology, validation, formal analysis, investigation, data curation, T.S.; Conceptualization, Methodology, resources, writing—review and editing, supervision, project administration, funding acquisition, M.Y. All authors have read and agreed to the published version of the manuscript.

Funding: This research was funded by JSPS KAKENHI (JP12852953 and JP18H05517), JST-CREST (15656567), and a project, “Moonshot Research and Development Program” (JPNP18016), commissioned by the New Energy and Industrial Technology Development Organization (NEDO).

Institutional Review Board Statement: Not applicable.

Informed Consent Statement: Not applicable.

Data Availability Statement: The data are contained within the article or Supplementary Materials.

Conflicts of Interest: The authors declare no conflict of interest.

References

1. Kibria, M.G.; Edwards, J.P.; Gabardo, C.M.; Dinh, C.T.; Seifitokaldani, A.; Sinton, D.; Sargent, E.H. Electrochemical CO_2 Reduction into Chemical Feedstocks: From Mechanistic Electrocatalysis Models to System Design. *Adv. Mater.* **2019**, *31*, e1807166. [CrossRef] [PubMed]
2. Nitopi, S.; Bertheussen, E.; Scott, S.B.; Liu, X.; Engstfeld, A.K.; Horch, S.; Seger, B.; Stephens, I.E.L.; Chan, K.; Hahn, C.; et al. Progress and Perspectives of Electrochemical CO_2 Reduction on Copper in Aqueous Electrolyte. *Chem. Rev.* **2019**, *119*, 7610–7672. [CrossRef] [PubMed]
3. Peterson, A.A.; Abild-Pedersen, F.; Studt, F.; Rossmeisl, J.; Nørskov, J.K. How copper catalyzes the electroreduction of carbon dioxide into hydrocarbon fuels. *Energy Environ. Sci.* **2010**, *3*, 1311–1315. [CrossRef]
4. Wang, Y.F.; Chen, Z.; Han, P.; Du, Y.H.; Gu, Z.X.; Xu, X.; Zheng, G.F. Single-Atomic Cu with Multiple Oxygen Vacancies on Ceria for Electrocatalytic CO_2 Reduction to CH_4. *ACS Catal.* **2018**, *8*, 7113–7119. [CrossRef]
5. Xu, Y.; Li, F.W.; Xu, A.N.; Edwards, J.P.; Hung, S.F.; Gabardo, C.M.; O’Brien, C.P.; Liu, S.J.; Wang, X.; Li, Y.H.; et al. Low coordination number copper catalysts for electrochemical CO_2 methanation in a membrane electrode assembly. *Nat. Commun.* **2021**, *12*, 4–10. [CrossRef] [PubMed]
6. Varela, A.S.; Ju, W.; Strasser, P. Molecular Nitrogen–Carbon Catalysts, Solid Metal Organic Framework Catalysts, and Solid Metal/Nitrogen-Doped Carbon (MNC) Catalysts for the Electrochemical CO_2 Reduction. *Adv. Energy Mater.* **2018**, *8*, 1703614. [CrossRef]

7. Yin, J.L.; Gao, Z.Y.; Wei, F.Y.; Liu, C.; Gong, J.; Li, J.M.; Li, W.Z.; Li, X.; Wang, G.W.; Lu, J.T.; et al. Customizable CO_2 Electroreduction to C_1 or C_{2+} Products through Cu_y/CeO_2 Interface Engineering. *ACS Catal.* **2022**, *12*, 1004–1011. [CrossRef]
8. Gao, D.F.; Zhang, Y.; Zhou, Z.W.; Cai, F.; Zhao, X.F.; Huang, W.; Li, Y.S.; Zhu, J.F.; Liu, P.; Yang, F.; et al. Enhancing CO_2 Electroreduction with the Metal–Oxide Interface. *J. Am. Chem. Soc.* **2017**, *139*, 5652–5655. [CrossRef]
9. Nakata, K.; Fujishima, A. TiO_2 photocatalysis: Design and applications. *J. Photochem. Photobiol. C Photochem. Rev.* **2012**, *13*, 169–189. [CrossRef]
10. Watanabe, R.; Yamauchi, M.; Sadakiyo, M.; Abe, R.; Takeguchi, T. CO_2-free electric power circulation via direct charge and discharge using the glycolic acid/oxalic acid redox couple. *Energy Environ. Sci.* **2015**, *8*, 1456–1462. [CrossRef]
11. Sadakiyo, M.; Hata, S.; Cui, X.; Yamauchi, M. Electrochemical Production of Glycolic Acid from Oxalic Acid Using a Polymer Electrolyte Alcohol Electrosynthesis Cell Containing a Porous TiO_2 Catalyst. *Sci. Rep.* **2017**, *7*, 17032. [CrossRef] [PubMed]
12. Sadakiyo, M.; Hata, S.; Fukushima, T.; Juhász, G.; Yamauchi, M. Electrochemical hydrogenation of non-aromatic carboxylic acid derivatives as a sustainable synthesis process: From catalyst design to device construction. *Phys. Chem. Chem. Phys.* **2019**, *21*, 5882–5889. [CrossRef] [PubMed]
13. Yamauchi, M.; Hata, S.; Eguchi, H.; Kitano, S.; Fukushima, T.; Higashi, M.; Sadakiyo, M.; Kato, K. Catalytic enhancement on Ti-Zr complex oxide particles for electrochemical hydrogenation of oxalic acid to produce an alcoholic compound by controlling electronic states and oxide structures. *Catal. Sci. Technol.* **2019**, *9*, 6561. [CrossRef]
14. Fukushima, T.; Yamauchi, M. Electrosynthesis of amino acids from biomass-derivable acids on titanium dioxide. *Chem. Commun.* **2019**, *55*, 14721–14724. [CrossRef] [PubMed]
15. Yamauchi, M. Inorganic Nanocatalysts for Hydrogenation Reactions Contributable to a Sustainable Material Supply. *Chem. Lett.* **2021**, *50*, 1901–1908. [CrossRef]
16. Eguchi, H.; Kato, K.; Juhasz, G.; Yamauchi, M. Selectivity enhancement in the electrochemical reduction of oxalic acid over titanium dioxide nanoparticles achieved by shape and energy-state control. *Catal. Sci. Technol.* **2021**, *11*, 7592–7597. [CrossRef]
17. Isegawa, M.; Staykov, A.; Yamauchi, M. Proton-Coupled Electron Transfer in Electrochemical Alanine Formation from Pyruvic Acid: Mechanism of Catalytic Reaction at the Interface between TiO_2(101) and Water. *J. Phys. Chem. C* **2021**, *125*, 12603–12613. [CrossRef]
18. Fukutani, K.; Yoshinobu, J.; Yamauchi, M.; Shima, T.; Orimo, S. Hydrogenomics: Efficient and Selective Hydrogenation of Stable Molecules Utilizing Three Aspects of Hydrogen. *Catal. Lett.* **2021**. [CrossRef]
19. Paola, A.D.; Bellardita, M.; Palmisano, L. Brookite, the Least Known TiO_2 Photocatalyst. *Catalysts* **2013**, *3*, 36–73. [CrossRef]
20. Zhao, B.; Chen, F.; Jiao, Y.; Zhang, J. Phase transition and morphological evolution of titania/titanate nanomaterials under alkalescent hydrothermal treatment. *J. Mater. Chem.* **2010**, *20*, 7990–7997. [CrossRef]
21. Haider, Z.; Kang, Y.S. Facile Preparation of Hierarchical TiO_2 Nano Structures: Growth Mechanism and Enhanced Photocatalytic H_2 Production from Water Splitting Using Methanol as a Sacrificial Reagent. *ACS Appl. Mater. Interfaces* **2014**, *6*, 10342–10352. [CrossRef] [PubMed]
22. Shannon, R.D. Revised effective ionic radii and systematic studies of interatomic distances in halides and chalcogenides. *Acta Cryst.* **1976**, *A32*, 751–767. [CrossRef]
23. Tauc, J.; Grigorovici, R.; Vancu, A. Optical Properties and Electronic Structure of Amorphous Germanium. *Phys. Status Solidi* **1966**, *15*, 627–637. [CrossRef]
24. Davis, E.A.; Mott, N.F. Conduction in non-crystalline systems V. Conductivity, optical absorption and photoconductivity in amorphous semiconductors. *Philos. Mag.* **1970**, *22*, 903–922. [CrossRef]
25. Reyes-Coronado, D.; Rodríguez-Gattorno, G.; Espinosa-Pesqueira, M.E.; Cab, C.; De Coss, R.; Oskam, G. Phase-pure TiO_2 nanoparticles: Anatase, brookite and rutile. *Nanotechnology* **2008**, *19*, 145605. [CrossRef]
26. Choudhury, B.; Dey, M.; Choudhury, A. Defect generation, d-d transition, and band gap reduction in Cu-doped TiO_2 nanoparticles. *Int. Nano Lett.* **2013**, *3*, 25. [CrossRef]
27. Pascher, T.F.; Ončák, M.; van der Linde, C.; Beyer, M.K. UV/Vis Spectroscopy of Copper Formate Clusters: Insight into Metal-Ligand Photochemistry. *Chem.-A Eur. J.* **2020**, *26*, 8286–8295. [CrossRef]
28. Desario, P.A.; Pietron, J.J.; Brintlinger, T.H.; McEntee, M.; Parker, J.F.; Baturina, O.; Stroud, R.M.; Rolison, D.R. Oxidation-stable plasmonic copper nanoparticles in photocatalytic TiO_2 nanoarchitectures. *Nanoscale* **2017**, *9*, 11720–11729. [CrossRef]
29. Tsuji, M.; Hikino, S.; Tanabe, R.; Sano, Y. Synthesis of Bicompartmental Ag/Cu Nanoparticles Using a Two-step Polyol Process. *Chem. Lett.* **2009**, *38*, 860–861. [CrossRef]
30. Amendola, V.; Meneghetti, M. Laser ablation synthesis in solution and size manipulation of noble metal nanoparticles. *Phys. Chem. Chem. Phys.* **2009**, *11*, 3805–3821. [CrossRef]
31. Cano, E.; Torres, C.L.; Bastidas, J.M. An XPS study of copper corrosion originated by formic acid vapour at 40% and 80% relative humidity. *Mater. Corros.* **2001**, *52*, 667–676. [CrossRef]
32. Ethiraj, A.S.; Kang, D.J. Synthesis and characterization of CuO nanowires by a simple wet chemical method. *Nanoscale Res. Lett.* **2012**, *7*, 70. [CrossRef] [PubMed]
33. Biesinger, M.C.; Lau, L.W.M.; Gerson, A.R.; Smart, R.S.C. Resolving surface chemical states in XPS analysis of first row transition metals, oxides and hydroxides: Sc, Ti, V, Cu and Zn. *Appl. Surf. Sci.* **2010**, *257*, 887–898. [CrossRef]
34. Idriss, H. On the wrong assignment of the XPS O1s signal at 531–532 eV attributed to oxygen vacancies in photo- and electro-catalysts for water splitting and other materials applications. *Surf. Sci.* **2021**, *712*, 121894. [CrossRef]

35. Kenausis, G.L.; Vörös, J.; Elbert, D.L.; Huang, N.; Hofer, R.; Ruiz-Taylor, L.; Textor, M.; Hubbell, J.A.; Spencer, N.D. Poly(L-lysine)-g-poly(ethylene glycol) layers on metal oxide surfaces: Attachment mechanism and effects of polymer architecture on resistance to protein adsorption. *J. Phys. Chem. B* **2000**, *104*, 3298–3309. [CrossRef]
36. Chalastara, K.; Guo, F.; Elouatik, S.; Demopoulos, G.P. Tunable Composition Aqueous-Synthesized. *Catalyst* **2020**, *10*, 407. [CrossRef]
37. Itai, T.; Takahashi, Y.; Uruga, T.; Tanida, H.; Iida, A. Selective detection of Fe and Mn species at mineral surfaces in weathered granite by conversion electron yield X-ray absorption fine structure. *Appl. Geochem.* **2008**, *23*, 2667–2675. [CrossRef]
38. DuBois, J.L.; Mukherjee, P.; Stack, T.D.P.; Hedman, B.; Solomon, E.I.; Hodgson, K.O. A systematic K-edge X-ray absorption spectroscopic study of Cu(III) sites. *J. Am. Chem. Soc.* **2000**, *122*, 5775–5787. [CrossRef]
39. Todaro, M.; Sciortino, L.; Gelardi, F.M.; Buscarino, G. Determination of geometry arrangement of copper ions in HKUST-1 by XAFS during a prolonged exposure to air. *J. Phys. Chem. C* **2017**, *121*, 24853–24860. [CrossRef]
40. Prestipino, C.; Regli, L.; Vitillo, J.G.; Bonino, F.; Damin, A.; Lamberti, C.; Zecchina, A.; Solari, P.L.; Kongshaug, K.O.; Bordiga, S. Local structure of framework Cu(II) in HKUST-1 metallorganic framework: Spectroscopic characterization upon activation and interaction with adsorbates. *Chem. Mater.* **2006**, *18*, 1337–1346. [CrossRef]
41. Shinagawa, T.; Larrazábal, G.O.; Martín, A.J.; Krumeich, F.; Pérez-Ramírez, J. Sulfur-Modified Copper Catalysts for the Electrochemical Reduction of Carbon Dioxide to Formate. *ACS Catal.* **2018**, *8*, 837–844. [CrossRef]
42. Kim, S.; Dong, W.J.; Gim, S.; Sohn, W.; Park, J.Y.; Yoo, C.J.; Jang, J.Y.; Lee, J.-L. Shape-controlled bismuth nanoflakes as highly selective catalysts for electrochemical carbon dioxide reduction to formate. *Nano Energy* **2017**, *39*, 44–52. [CrossRef]
43. Zheng, T.T.; Jiang, K.; Ta, N.; Hu, Y.F.; Zeng, J.; Liu, J.Y.; Wang, H.T. Large-Scale and Highly Selective CO_2 Electrocatalytic Reduction on Nickel Single-Atom Catalyst. *Joule* **2019**, *3*, 265–278. [CrossRef]
44. Xue, L.; Zhang, C.; Wu, J.; Fan, Q.Y.; Liu, Y.; Wu, Y.; Li, J.; Zhang, H.; Liu, F.; Zeng, S. Unveiling the reaction pathway on Cu/CeO_2 catalyst for electrocatalytic CO_2 reduction to CH_4. *Appl. Catal. B Environ.* **2022**, *304*, 120951. [CrossRef]
45. Varandili, S.B.; Huang, J.; Oveisi, E.; Gregorio, G.L.D.; Mensi, M.; Strach, M.; Vavra, J.; Gadiyar, C.; Bhowmik, A.; Buonsanti, R. Synthesis of Cu/CeO_{2-x} Nanocrystalline Heterodimers with Interfacial Active Sites To Promote CO_2 Electroreduction. *ACS Catal.* **2019**, *9*, 5035–5046. [CrossRef]
46. Huygh, S.; Bogaerts, A.; Neyts, E.C. How Oxygen Vacancies Activate CO_2 Dissociation on TiO_2 Anatase (001). *J. Phys. Chem. C* **2016**, *120*, 21659–21669. [CrossRef]
47. Kato, K.; Tanaka, H. Visualizing charge densities and electrostatic potentials in materials by synchrotron X-ray powder diffraction. *Adv. Phys. X* **2016**, *1*, 55–80. [CrossRef]
48. Ravel, B.; Newville, M. ATHENA, ARTEMIS, HEPHAESTUS: Data analysis for X-ray absorption spectroscopy using IFEFFIT. *J. Synchrotron Radiat.* **2005**, *12*, 537–541. [CrossRef]
49. Niu, S.; Li, S.; Du, Y.; Han, X.; Xu, P. How to Reliably Report the Overpotential of an Electrocatalyst. *ACS Energy Lett.* **2020**, *5*, 1083–1087. [CrossRef]
50. Zhang, T.; Verma, S.; Kim, S.; Fister, T.T.; Kenis, P.J.A.; Gewirth, A.A. Highly dispersed, single-site copper catalysts for the electroreduction of CO_2 to methane. *J. Electroanal. Chem.* **2020**, *875*, 113862. [CrossRef]
51. Guan, A.X.; Chen, Z.; Quan, Y.L.; Peng, C.; Wang, Z.Q.; Sham, T.-K.; Yang, C.; Ji, Y.L.; Qian, L.P.; Xu, X.; et al. Boosting CO_2 Electroreduction to CH_4 via Tuning Neighboring Single-Copper Sites. *ACS Energy Lett.* **2020**, *5*, 1044–1053. [CrossRef]
52. Chen, S.H.; Wang, B.Q.; Zhu, J.X.; Wang, L.Q.; Ou, H.H.; Zhang, Z.D.; Liang, X.; Zheng, L.R.; Zhou, L.; Su, Y.-Q.; et al. Lewis Acid Site-Promoted Single-Atomic Cu Catalyzes Electrochemical CO_2 Methanation. *Nano Lett.* **2021**, *21*, 7325–7331. [CrossRef] [PubMed]
53. Guan, A.X.; Yang, C.; Wang, Q.H.; Qian, L.P.; Cao, J.Y.; Zhang, L.J.; Wu, M.L.; Zheng, G.F.; Zhou, L.; Su, Y.-Q.; et al. DAtomic-Level Copper Sites for Selective CO_2 Electroreduction to Hydrocarbon. *ACS Sustain. Chem. Eng.* **2021**, *9*, 13536–13544. [CrossRef]